Available online at www.sciencedirect.com
ScienceDirect
Trans. Nonferrous Met. Soc. China 33(2023) 714−727
Transactions of Nonferrous Metals Society of China
www.tnmsc.cn

Effects of bimodal basal texture on bending stress and microstructure evolution of Mg−2.6Nd−0.55Zn−0.5Zr alloys

Wen-cong ZHANG, Yu-xuan LIU, Jun-fei MA, Wen-ke WANG, Wen-zhen CHEN, Xin-tong LIU, Jian-lei YANG

School of Materials Science and Engineering, Harbin Institute of Technology at Weihai, Weihai 264209, China

Received 16 November 2021; accepted 25 April 2022

Abstract: The extrusion direction (ED) and transverse direction (TD) samples were cut from Mg−2.6Nd−0.55Zn−0.5Zr alloy sheet, and the effects of bimodal basal texture on the bending stress and microstructure evolution were investigated. Results showed that the ED sample with weak basal texture possessed much lower bending stress than the TD sample. This anisotropy is attributed to the role of different textures on the evolution of deformation mechanisms and microstructures. For the ED sample with weak basal texture, the dominant deformation mechanisms were basal slip in the majority with minor supplement of $\{10\bar{1}2\}$ tension twin in the inner region while basal slip and prismatic slip in the outer region. In comparison, the TD sample with strong basal texture activated more $\{10\bar{1}2\}$ tension twin in the inner region and more prismatic slip in the outer region. The activation of $\{10\bar{1}2\}$ tension twin promoted the development of $\langle 0002\rangle$//compression direction type texture with the confined ±30° angle range in the inner region and reduced the emergence propensity of high dislocation density and low angle grain boundaries. The massive activation of $\{10\bar{1}2\}$ tension twin allowed the TD sample to maintain a high strain-hardening capacity, which was the fundamental reason for the high bending stress in this sample.

Key words: Mg−Nd−Zn−Zr alloy; texture; tension twin; three-point bending; bending stress; microstructure evolution

1 Introduction

Magnesium (Mg) alloys have been widely used in aerospace, automotive and 3C products in recent years because of their low density, high specific strength and high stiffness [1−4]. However, due to their inherent hexagonal close packed (HCP) structures, deformed Mg alloy sheets usually produce strong basal texture during extrusion/rolling deformation, which results in strong anisotropy of mechanical behavior. WANG et al [5] discovered that strong texture in one direction of Mg alloy sheets was the key reason limiting their stretch formability in the bulging experiment with biaxial tension. Because the inner region was under compression mode and the outer region was under tension mode, this anisotropy would be more obvious during the bending process. Different deformation mechanisms of the inner and outer regions lead to differences in their bending stress and microstructure evolution of Mg alloy sheets. SINGH et al [6] found that E-Form Mg alloy with weaker basal texture showed better bendability and more prominent compression and double twins. Similarly, WANG et al [7] studied the bending process of ZK60 rolled sheets with fiber texture, and found that the transverse direction (TD) sample with weak texture exhibits lower bending stress and much less $\{10\bar{1}2\}$ tension twins.

Mg−Nd−Zn−Zr alloys have great potential in biomedical fields. During extrusion process, Mg−Nd−Zn−Zr alloys can form bimodal basal distribution of texture components [8]. However, bending of Mg−Nd−Zn−Zr alloys with bimodal basal texture has not been studied. Most of the

Corresponding author: Wen-ke WANG, Tel/Fax: +86-631-5672167, E-mail: 15B309020@hit.edu.cn
DOI: 10.1016/S1003-6326(22)66140-5

current studies on bending deformation have been focused on strong basal texture or extruded fiber texture. Importantly, the bimodal basal texture activated basal slip substantially in tension or compression test and reduced the generation of tension twins in compression test, leading to a reduction in tension−compression asymmetry [9]. This effect will be more complicated in the bending process due to the deformation that the inner region is under compression mode and the outer region is under tension mode. On the other hand, the addition of Nd element can greatly increase the activation ratio of non-basal slip systems and lead to significant mechanical changes [10]. These will affect the process parameters setting of Mg−Nd− Zn−Zr alloy in the design of the bending process. Therefore, in order to expand the application of Mg−Nd−Zn−Zr alloy, it is necessary to investigate the effect of texture on the bending process of Mg−Nd−Zn−Zr alloy. For this reason, in this work, we investigated the effect of bimodal basal texture on the anisotropy of bending stress and the microstructure evolution during bending process for Mg−Nd−Zn−Zr alloys by using Mg−2.6Nd−0.55Zn−0.5Zr extrusion sheets as the initial material.

2 Experimental

The initial material used for this study was the extruded Mg−Nd−Zn−Zr alloy sheets with a thickness of 5 mm. Rectangular samples (Fig. 1(a)) with dimensions of 50 mm (Length) × 20 mm (Width) × 5 mm (Thickness) were cut from the extruded sheets along the extrusion direction (ED) and TD, and referred as the ED sample and the TD sample, respectively. The sample surfaces were polished by abrasive paper (400, 600 and 800 grit) to eliminate oxide layers and surface stress concentrations. As shown in Fig. 1(b), the final bending angles of both ED and TD samples were ~136°. Three-point bending test was performed on an Instron 5967 machine equipped with a three-point bending system (as shown in Fig. 1(c)). The diameter of the bending punch was 10 mm, the distance between two supports was 30 mm, and the test speed was 0.5 mm/min. Bluehill software (from Instron 5967) was used to record the bending loading−position curve. In addition, uniaxial tension and compression tests were also conducted on an Instron 5967 machine at a constant strain rate of $1\times10^{-3}\ s^{-1}$ at room temperature. Tension samples with dimensions of 15 mm in gauge length and 4 mm in width and compression samples with dimensions of 3 mm in diameter and 4.5 mm in length were both cut from extruded sheets along the ED and TD. To ensure that the results were true and reliable, each group of experiments were repeated three times.

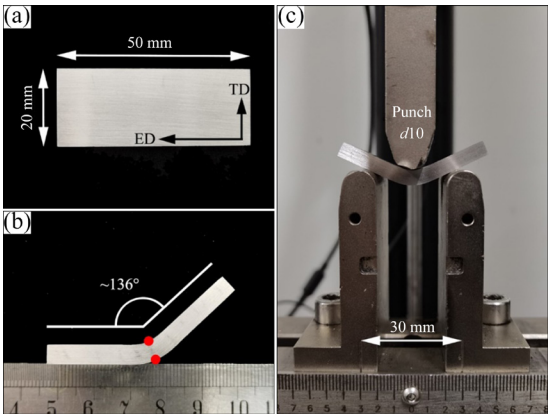

Fig. 1 physical maps of bending process: (a) Sample size; (b) Final bending angle; (c) Experimental device

The microstructure characterization was performed by electron backscattered diffraction (EBSD). The samples were prepared via standard metallography, mechanically polished using soft diamond, followed by electropolishing at 0.25 A for 8 min in a 5:3 (volume ratio) solution of C_2H_6O and H_3PO_4. Microstructures after bending were measured on the ED−ND (ND is the normal direction) plane for the ED sample and on the TD−ND plane for the TD sample using a scanning electron microscope (Zeiss) equipped with the EBSD system and TSL-OIM™ (TexSEM Laboratories orientation imaging microscopy) software. Both inner region and outer region of samples were selected as observation areas. For the microstructure analysis of the bending samples, the scanned area and measurement step size were 103.5 μm × 78.46 μm and 0.3 μm, respectively. The acceleration voltage was 20 keV, while the working distance and the sample tilt angle were set to be 15 mm and 70°, respectively. The EBSD analysis was conducted on data with an average confidence index (CI) of more than 0.1. The CI is a relevant measure of statistical quality in EBSD indexing. EBSD technique was used to analyze the evolution of microstructure and texture that occurred along the thickness direction.

3 Results and discussion

3.1 Microstructure characteristics of extruded Mg−2.6Nd−0.55Zn−0.5Zr alloy

Figure 2(a) revealed the microstructure characteristics of the initial material, i.e., the extruded Mg−2.6Nd−0.55Zn−0.5Zr alloy sheets. The corresponding data of grain size distribution and length-to-diameter ratio were shown in Figs. 2(b, c), respectively. It could be clearly seen that the initial material exhibited a uniform equiaxed-grain structure with the average grain size of about 4.16 μm. In addition, the grain size distribution could be well fitted by the Gaussian function, indicating good initial microstructure homogeneity. Figure 2(d) showed that the initial sheets possess relatively few internal defects. HAGBs (HAGB: high angle grain boundaries ranging from 15° to 180°) accounted for 91.6%. These results showed that the initial microstructure was relatively homogeneous. The difference in grain size between two directions was small. This provided a guarantee to study the effect of texture on the anisotropy of bending stress and the microstructure evolution during bending process.

The texture of the extruded Mg−2.6Nd−0.55Zn−0.5Zr alloy sheets was shown in Fig. 2(e), which provided the measured (0002), $(10\bar{1}0)$ and $(11\bar{2}0)$ pole figures of the initial sheets. It was clearly that the initial texture state showed a bimodal distribution along the ED with a maximal intensity of about 9.286. According to Ref. [11], this texture state was generally caused by the addition of Nd and Zn elements to the alloy. In order to more clearly describe the initial texture state and intensity distribution, the (0002) Times Random values along the ED and TD were obtained from the (0002) pole figures in Fig. 2(e), respectively. The normalized (0002) pole density was obtained by the Times Random values divided by $\int_0^{\pi/2} I_{\text{intensity}} \cos\alpha \mathrm{d}\alpha$ ($I_{\text{intensity}}$ is the intensity of

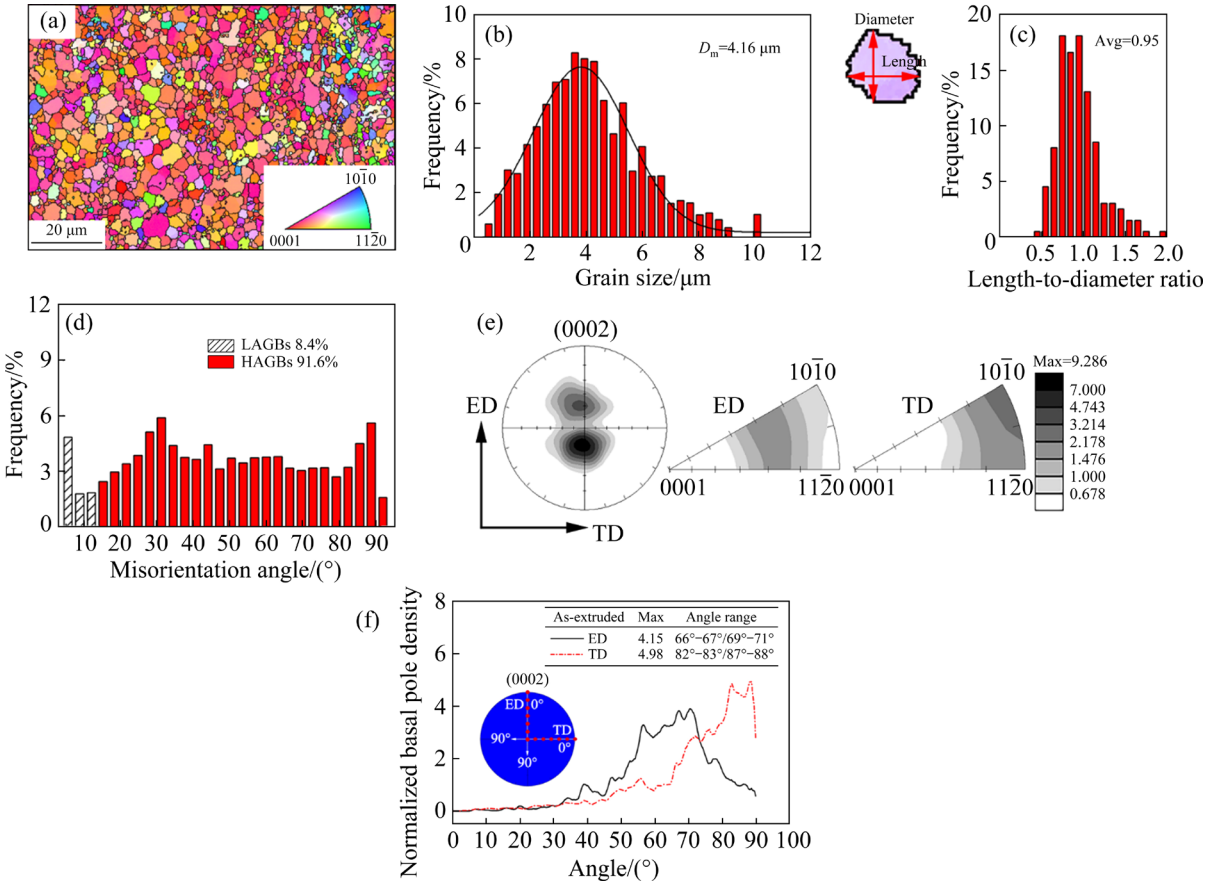

Fig. 2 Microstructure characteristics and texture state of extruded Mg−Nd−Zn−Zr alloy sheets in ED−TD plane: (a) IPF (inverse pole figure); (b, c) Grain size and length-to-diameter ratio distribution, respectively; (d) Misorientation angle distribution; (e) {0002} basal plane pole figures; (f) (0002) pole density distribution along ED and TD

orientation distribution, and α is the angle from the ED or the TD), as shown in Fig. 2(f). From Fig. 2(f), it could be found that the initial texture of the ED sample was significantly different from that of the TD sample. Compared with the ED sample, the basal plane distribution of the TD sample was more concentrated. The basal pole density of the ED was widely distributed in the range of 66°−71°, while that of the TD was concentrated in the range of 82°−88°.

3.2 Bending behavior

The mechanical properties and anisotropy of the ED and TD samples could be seen by stress−strain curves of tension and compression tests in Fig. 3(a). The compressive yield strength of the TD sample was higher than that of the ED sample. According to Refs. [12,13], this was mainly attributed to differences in the initial texture: more

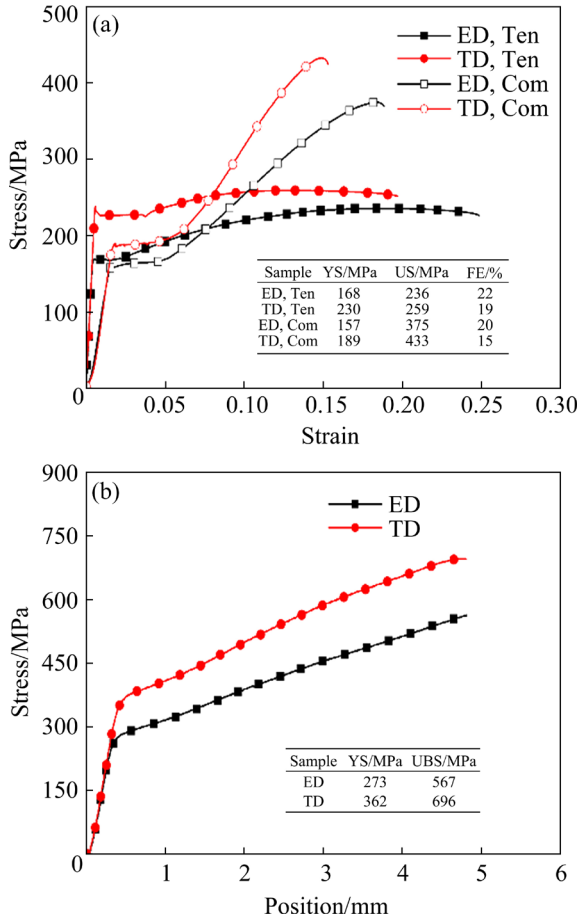

Fig. 3 Stress−strain curves during tension and compression deformation (a) and stress−position curves during bending process (b) for ED and TD samples at room temperature (Ten: Tension test; Com: Compression test; YS: Yield strength; US: Ultimate strength; FE: Fracture elongation; UBS: Ultimate bending strength)

grains were favorable for the activation of $\{10\bar{1}2\}$ tension twin than basal slip in the TD sample while less in the ED sample. The critical resolved shear stress (CRSS) for basal slip was much lower than that for $\{10\bar{1}2\}$ tension twin and non-basal slip [14]. Similarly, the tensile yield strength of the TD sample was also higher than that of the ED sample because of less orientation that favored basal slip. This was also due to the difference of initial texture.

Similarly, the inner region of the sample is under compression mode and the outer region is under tension mode during the bending process. Fig. 3(b) showed similar anisotropy during the bending process between the ED sample and the TD sample. It could be judged that the yield strength of the TD sample (362 MPa) was also higher than that of the ED sample (273 MPa) at the same bending angle during the bending process. This meant that the TD sample with strong basal texture exhibited higher bending stress. Based on the observations above, the initial material was essentially free of internal defects, and there was no difference in grain size along the two directions. That was to say, the significant difference in the initial texture of the Mg−2.6Nd−0.55Zn−0.5Zr sheet led to the asymmetry in the bending stress of the ED and the TD samples.

3.3 Microstructure characteristic after bending

The ED−ND plane in the ED sample and the TD−ND plane in the TD sample were measured using EBSD to observe the microstructure and texture. The outer region and the inner region of bending samples were selected as the observation area and marked as the ED/TD-Out and the ED/TD-In, respectively. Figures 4(a−d) showed the KAM (kernel average misorientation) maps of the inner region and the outer region in the ED sample and the TD sample, and it could be clearly seen that the degree of local strain and dislocation density of the inner region were lower than those of the outer region. This was because the inner region was under compression mode and the outer region was under the tension mode during the bending process. The deformation mechanism of the tension mode was dominated by dislocation slip. In contrast, that of the compression mode had a certain percentage of $\{10\bar{1}2\}$ tension twin whose activation would reduce the emergence propensity of high dislocation

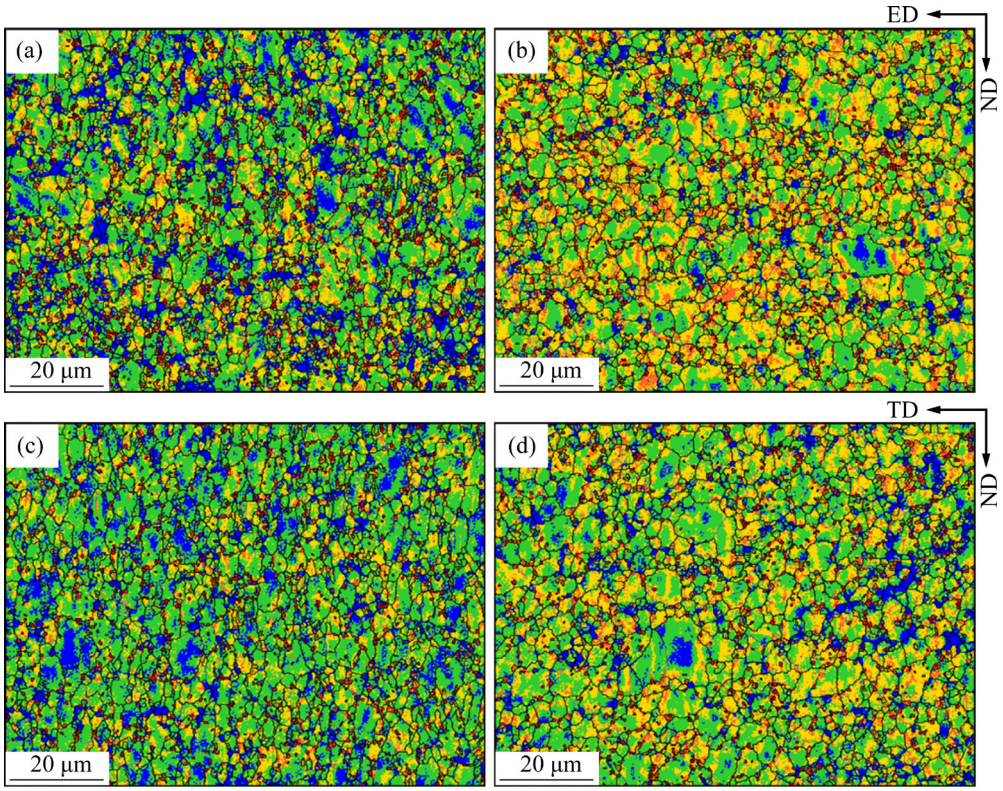

KAM	0−1	1−2	2−3	3−4	4−5
ED-In/%	19.3	47.9	22.2	4.9	5.7
ED-Out/%	6.8	40.4	37.1	10.6	5.1
TD-In/%	17.3	55.2	19.1	3.7	4.7
TD-Out/%	11.4	44.6	32.2	7.5	4.3

Fig. 4 KAM maps of ED and TD samples measured in inner and outer regions through thickness direction: (a) ED-In; (b) ED-Out; (c) TD-In; (d) TD-Out

density. It was worth noting that the dislocation density of the TD-In was lower than that of the ED-In. This implied that strong basal texture of the TD sample corresponded to more orientation favoring $\{10\bar{1}2\}$ tension twin instead of slip under the compression mode.

The EBSD microstructure characteristics of Figs. 5(a−d) supported the analysis of Fig. 4. According to the literature [15], when the compression direction was perpendicular to the *c*-axis, the *c*-axis $\{10\bar{1}2\}$ tension twins were oriented to only a limited range of angle, i.e., at ±30° along the compression direction (ED for ED specimens vs TD for TD specimens); in contrast, when the tension direction was parallel to the *c*-axis, the *c*-axis $\{10\bar{1}2\}$ tension twins were uniformly distributed in the ED−TD plane. Figure 5 illustrated boundaries of $\{10\bar{1}2\}$ tension twins and showed $\{10\bar{1}2\}$ tension twins together with original grains using crystal orientation. In the figure, the blue represented $\{10\bar{1}2\}$ tension twins; the red represented original grains. From Fig. 5, it could be seen that there were $\{10\bar{1}2\}$ tension twins in both the inner and outer regions. The $\{10\bar{1}2\}$ tension twins in the outer region of the sample might be caused by local stress concentration. The twinned volume fraction of the inner region was significantly higher than that of the outer region. This was attributed to the inhibition of twinning growth under the tension mode. Figures 5(a) and (c) showed that the twinned volume fraction of TD-In was lower than that of ED-In, which corresponded to the low dislocation density of TD-In in Fig. 4.

In order to further describe the inner region and the outer region microstructures of the samples after bending, Figs. 6(a−d) indicated the distribution of LAGBs (LAGB: low angle grain boundaries ranging from 0° to 15°) and the orientation of each grain by using the IPF. Firstly, compared with the initial sheet, it could be seen that

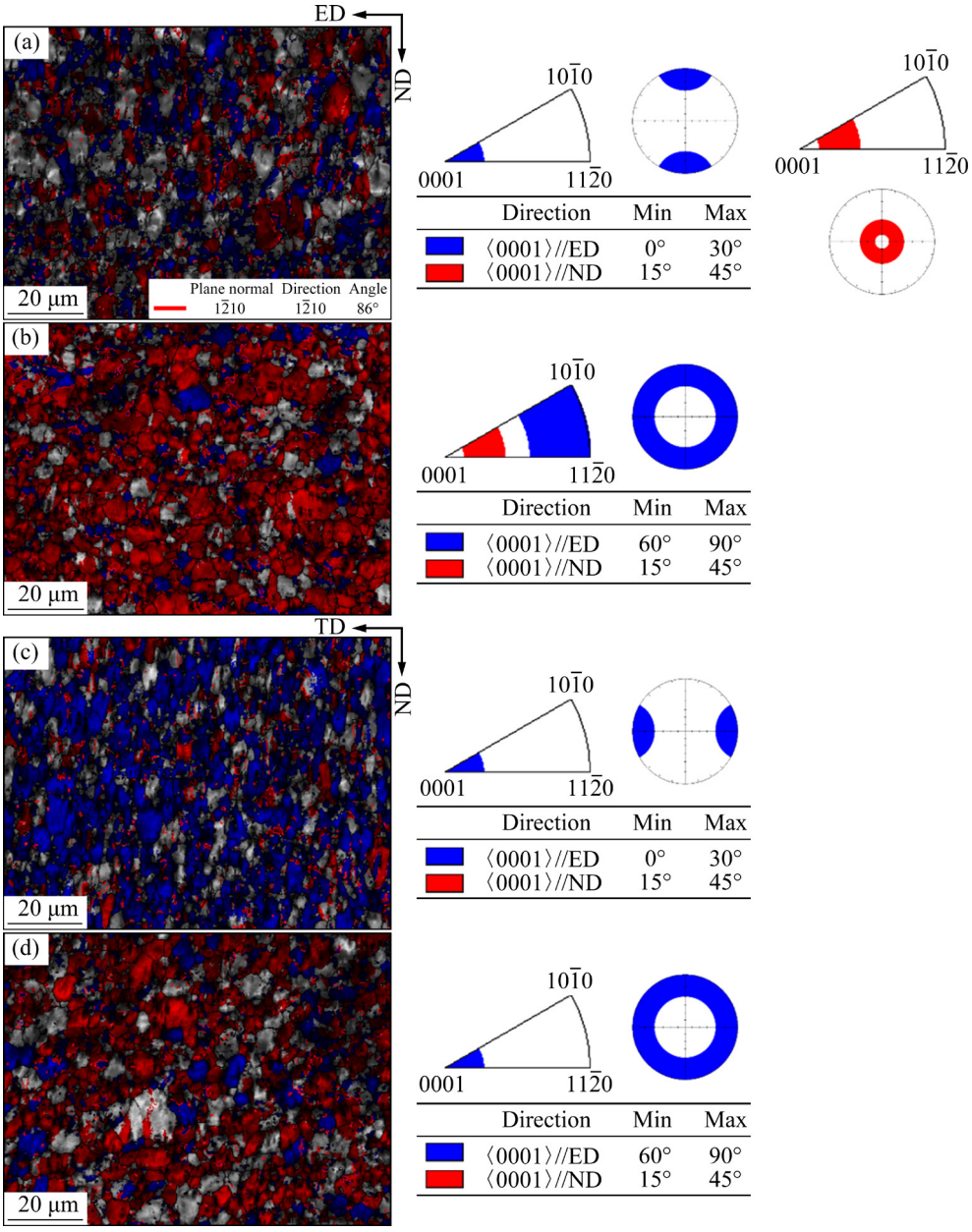

Fig. 5 {10$\bar{1}$2} tension twin and original grain in inner and outer regions of ED and TD samples: (a) ED-In; (b) ED-Out; (c) TD-In; (d) TD-Out

a large number of LAGBs appeared on both ED and TD samples after bending, which was caused by the activation of slip [16,17]. Figure 6(e) showed the fractions of LAGBs after the summary. It could be seen that the proportion of LAGBs in the inner region was significantly lower than that in the outer region, and the ED-Out had a higher percentage of LAGBs than the TD-Out. This further indicated that dislocation slip existed in both inner and outer regions and accounted for a higher percentage in the outer region under the tension mode. Compared with the TD sample, the ED sample with bimodal basal texture was more likely to activate basal slip under the tension mode. Slight increase of LAGBs in the TD-In might be ascribed to the twin boundaries generated by {10$\bar{1}$2} tension twins. Combined with Figs. 4−6, it could be judged that the differences in the initial texture during the bending process led to different microstructure evolutions. The strong basal texture of the TD sample (Fig. 2(e)) provided more grains favorable to the activation of {10$\bar{1}$2} tension twins under the compression mode and less orientations favorable to the basal slip under the tension mode compared with the ED sample, which led to a lower dislocation density and fewer LAGBs.

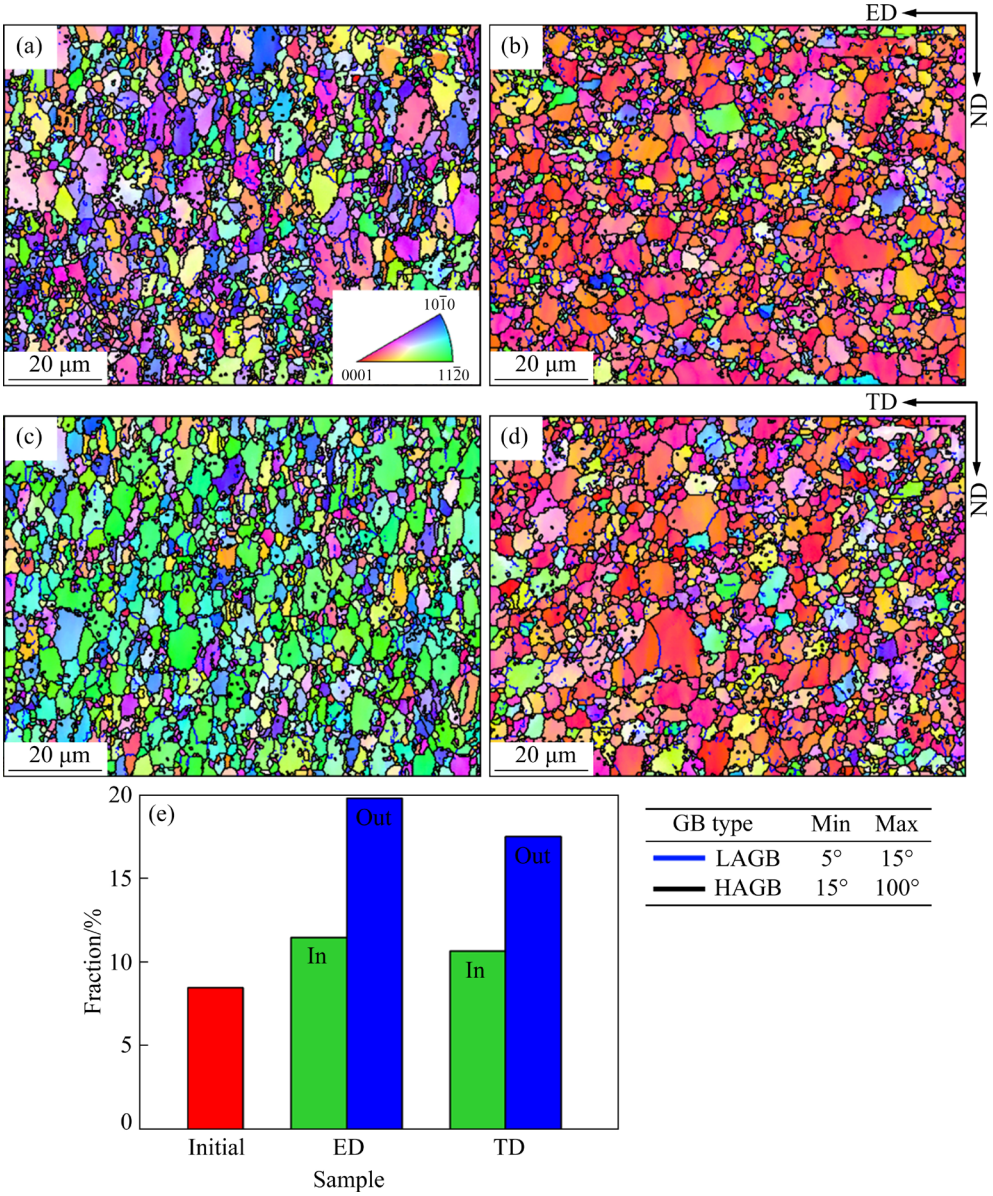

Fig. 6 Microstructure characteristics in inner and outer regions of ED and TD samples: (a) ED-In IPF; (b) ED-Out IPF; (c) TD-In IPF; (d) TD-Out IPF; (e) Fractions of LAGBs in initial material and different regions of bending samples

Secondly, through the color code within the unit triangle of IPF, it could be known that there were a large number of blue and green grains in the inner region, corresponding to $\langle 10\bar{1}0\rangle$//ND and $\langle 11\bar{2}0\rangle$//ND orientations, respectively. These orientations were the result of $\{10\bar{1}2\}$ tension twins under the compression mode [18]. Grain orientations in the outer region were similar to the initial state, retaining a large number of red grains, corresponding to $\langle 0001\rangle$//ND orientation. These orientations were the result of dislocation slip under the tension mode. In order to describe more clearly the changes of grain orientations during the bending process, the evolution of texture in the inner region and the outer region of the bending samples was studied and analyzed subsequently.

3.4 Texture characteristics after bending

Figure 7 showed the (0002), $(10\bar{1}0)$ and $(11\bar{2}0)$ pole figures in the inner region and the outer region of the ED sample and the TD sample after bending process. To compare with the initial texture conveniently, the measured results of the ED sample and the TD sample were rotated in the OIM software. Both the ED−ND plane in ED sample and the TD−ND plane in TD sample were transferred into the ED−TD plane. As described above in Fig. 2(f), the initial texture of the ED sample showed

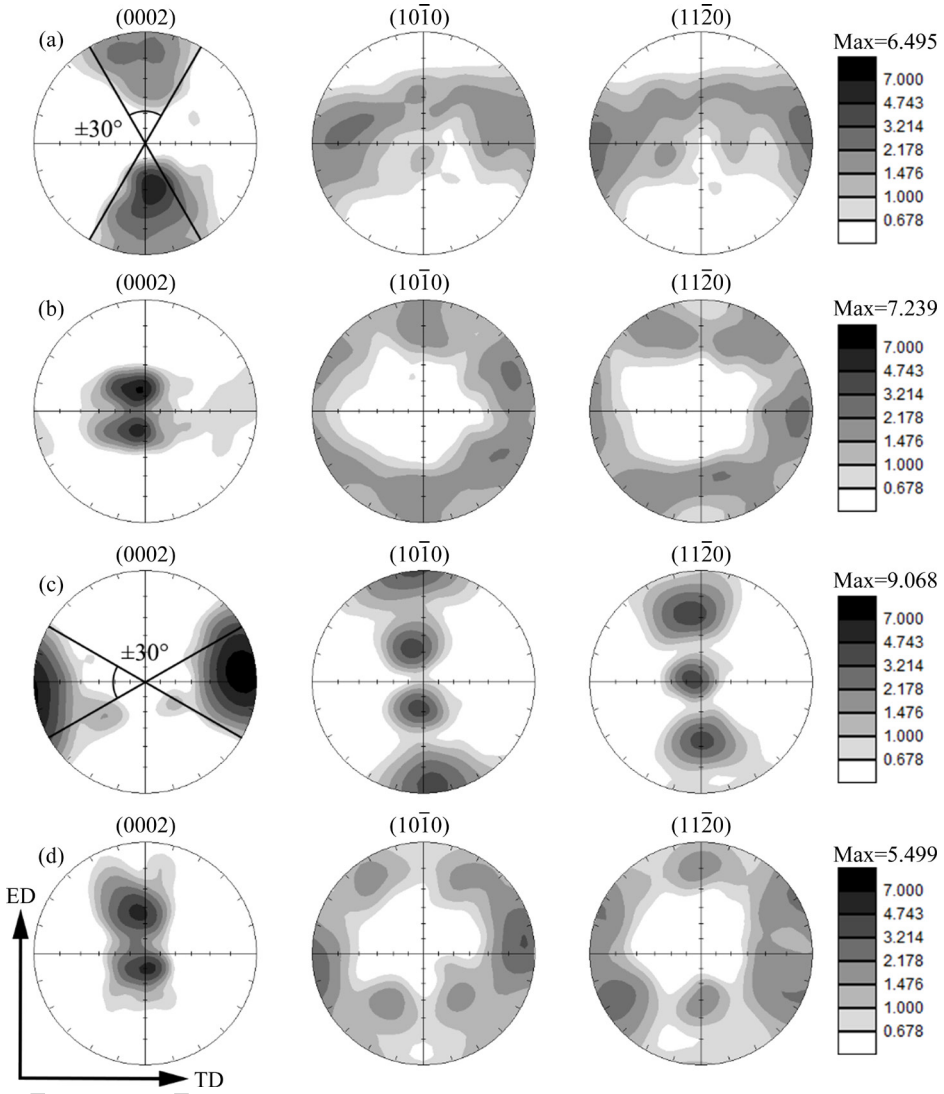

Fig. 7 (0002), (10$\bar{1}$0) and (11$\bar{2}$0) pole figures in different regions: (a) ED-In; (b) ED-Out; (c) TD-In; (d) TD-Out

a bimodal distribution state. That was to say, the ED sample with weak basal texture always had some grains favorable to the activation of basal slip no matter in compression mode of the inner region or in tension mode of the outer region. For compression along the ED in the ED-In, {10$\bar{1}$2} tension twin and basal slip could be both activated. It was well known that the {10$\bar{1}$2} tension twin could induce a crystallographic lattice reorientation of 86.3°. Therefore, a texture component with basal planes perpendicular to the ED was formed. It was worth noting that the *c*-axis parallel to the ED was placed in a limited angle range of ±30° from the ED to the TD. According to the literature [15], only one pair of {10$\bar{1}$2} tension twin variants had the highest Schmid factor value of 0.374−0.499 and was activated since the angle θ between the loading direction and the *a*-axis was in the range of 0°−30° when the compression direction was perpendicular to the *c*-axis. Moreover, the activation of basal slip under compression mode also promoted the *c*-axis to rotate toward the ED [19], which led to a large number of *c*-axes 45° away from the ND. Consequently, the combined effect of basal slip and {10$\bar{1}$2} tension twin contributed to the formation of texture as shown in Fig. 7(a).

To confirm the corresponding deformation mechanism of each region, the relationship between three crystal orientations of samples and the sample coordinate system was selected for in-depth analysis in this study, and Figures 8 and 9 were plotted. Figure 8 showed the blue, red and green colors for the grains with (0002), (10$\bar{1}$0) and (11$\bar{2}$0) crystal orientations parallel to the ED, respectively, and similarly Figure 9 showed the

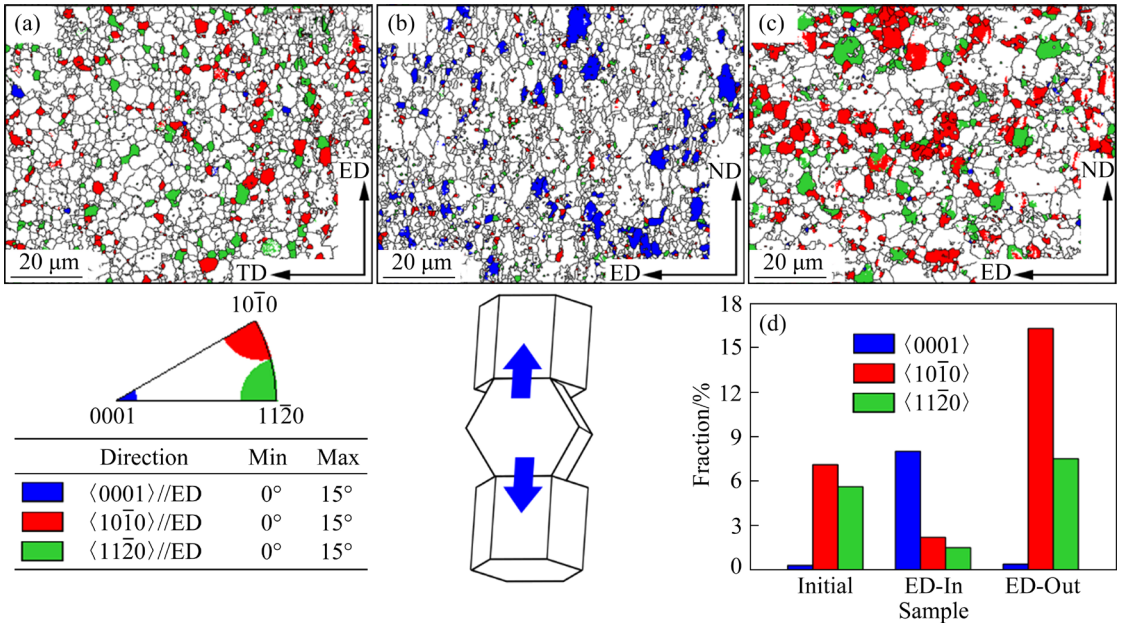

Fig. 8 Crystal orientation maps of ED samples: (a) Initial material; (b) ED-In; (c) ED-Out; (d) Fraction of grains in each orientation (Blue represents grains with ⟨0001⟩ in angle range of 0°−15° away from the ED, red represents grains with ⟨10$\bar{1}$0⟩ in the angle range of 0°−15° away from the ED, and green represents grains with ⟨11$\bar{2}$0⟩ in angle range of 0°−15° away from ED)

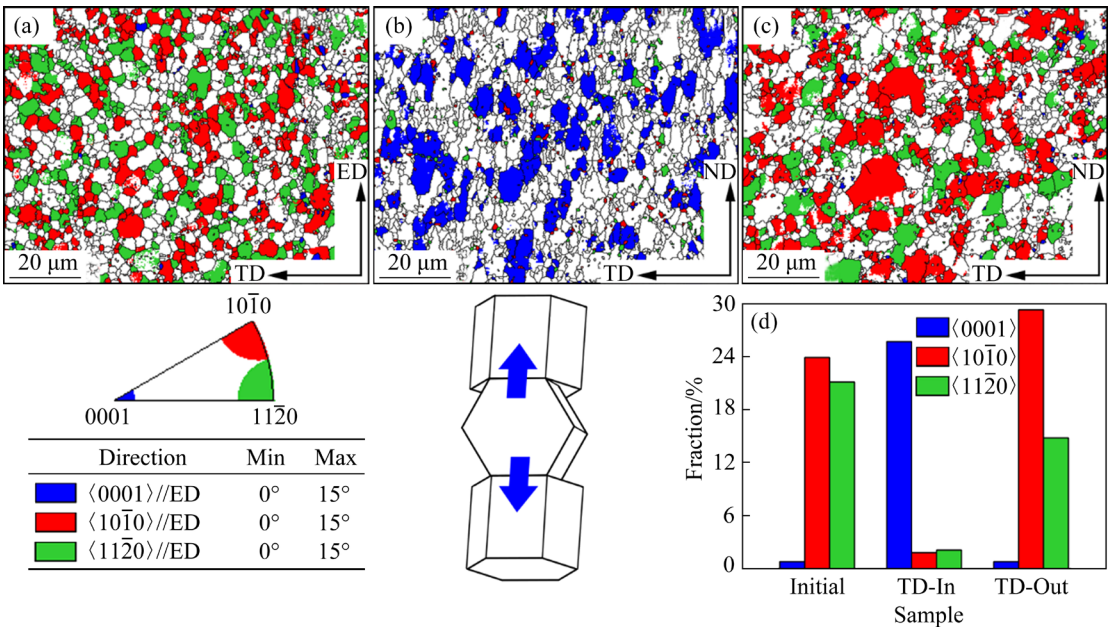

Fig. 9 Crystal orientation maps of TD samples: (a) Initial material; (b) TD-In; (c) TD-Out; (d) Fractions of grains in each orientation (Blue represents grains with ⟨0001⟩ in the angle range of 0°−15° away from the TD, red represents grains with ⟨10$\bar{1}$0⟩ in the angle range of 0°−15° away from the TD, and green represents grains with ⟨11$\bar{2}$0⟩ in angle range of 0°−15° away from TD)

grains with three orientations parallel to the TD. All tolerances were selected between 0° and 15°. It could be seen that the fraction of blue grains in the inner region increased significantly from 0.3% to 8%. This part could be judged as the crystal rotation caused by {10$\bar{1}$2} tension twin, and thus as the fraction of twinning occurrence.

In order to further estimate the fraction of each deformation mechanism for participating in the deformation, the relationship between slip system and the angle between loading direction and *c*-axis was introduced and plotted in Fig. 10 according

to Ref. [20]. GUAN et al [20] pointed out that under tension mode $\{10\bar{1}2\}$ tension twin was the main deformation mechanism for θ<23° (θ represents the angle between the loading direction and the c-axis), basal slip for θ=23°−77°, and prismatic slip for θ=77°−90°; while under compression mode, θ=67°−90° for $\{10\bar{1}2\}$ tension twin, θ=13°−67° for basal slip, and θ>13° for prismatic slip. As shown in Fig. 10, the grains favorable to basal slip were more than those for $\{10\bar{1}2\}$ tension twin. Combining with the Figs. 8 and 10, it could be seen that the deformation mechanism was dominated by basal slip and supplemented by tension twin when the ED-In was under the compression mode, corresponding to the results observed in Fig. 7(a).

Due to the initial texture of the ED sample, the basal slip could also be activated when the ED-Out was under the tension mode. In the ED-Out, the (0002) poles retained the bimodal distribution with the bimodal angle narrowing from 45° to 30° compared with the initial material. Moreover, both $(10\bar{1}0)$ and $(11\bar{2}0)$ pole figures showed six-fold symmetry in the ED-Out during the bending process. According to Refs. [2,21], it was known that the prismatic slip resulted in a rotation of the $(10\bar{1}0)$ plane around the c-axis to parallel to the tension deformation loading direction. As shown in Fig. 8, the fraction of grains with $\langle 10\bar{1}0\rangle$ pole parallel to the ED which was the tension deformation

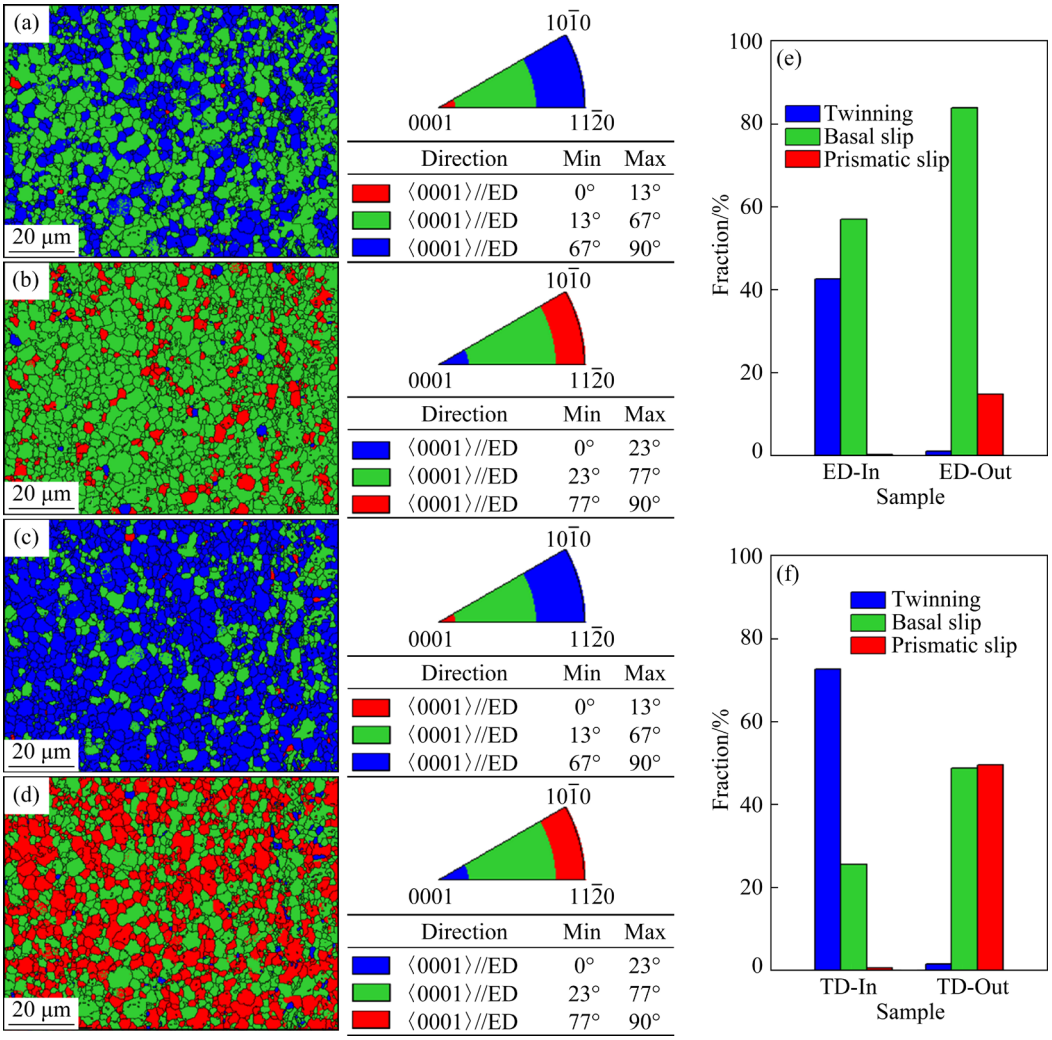

Fig. 10 Orientation distributions of Mg−Nd−Zn−Zr alloys at different states using crystal direction maps: (a, b) Compression and tension deformation along ED, respectively; (c, d) Compression and tension deformation along TD, respectively; (e, f) Fractions of different states in ED and TD samples, respectively (In crystal direction map, the grains with ⟨0001⟩ in angle ranges of 0°−23°, 23°−77° and 77°−90° away from the tension direction were depicted by blue, green and red colors, respectively, and the grains with the ⟨0001⟩ in angle ranges of 0°−13°, 13°−67° and 67°−90° away from compression direction were depicted by red, green and blue colors, respectively)

direction in the ED-Out increased significantly to 16.3% compared with initial material. Figure 10 showed that basal slip and prismatic slip could be activated during the bending process in the outer region, and basal slip combined with prismatic slip was the deformation mechanism in the ED-Out but basal slip was also the dominant.

In contrast to the ED sample, the texture in the TD sample was more concentrated. That was to say, the TD sample with strong basal texture had more grains favoring the activation of $\{10\bar{1}2\}$ tension twin under the compression mode of the inner region. As shown in Fig. 7(c), the effect of $\{10\bar{1}2\}$ tension twin contributed to the formation of strong twin texture with the *c*-axis parallel to the TD. Similar to the ED-In, the *c*-axes in the TD-In were placed in a confined angle range of ±30° from the TD toward the ED due to the compression mode. From the $(10\bar{1}0)$ and $(11\bar{2}0)$ pole figures, it could be seen that $(10\bar{1}0)$ and $(11\bar{2}0)$ planes were transversely symmetrical about the sheet, which could be characterized by a strong $(11\bar{2}0)\langle 10\bar{1}0\rangle$ texture [22,23]. This result was also caused by the specific $\{10\bar{1}2\}$ tension twin variants under the compression mode. The activation of $\{10\bar{1}2\}$ tension twin was confirmed again in Fig. 9 which presented a significantly high fraction for $\{10\bar{1}2\}$ tension twin. Figure 10 showed that basal slip could be activated in the TD-In while $\{10\bar{1}2\}$ tension twin was in the dominant position. Therefore, combined with Figs. 9 and 10, it could be judged that the prior deformation mechanism of the TD-In was $\{10\bar{1}2\}$ tension twin in the majority with minor supplement of basal slip.

Because of the texture characteristic in the TD sample, it had less grains favoring the activation of basal slip and more grains favoring the activation of prismatic slip when the TD-Out was under tension mode. In the TD-Out, the bimodal angle maintained 45° and more $\langle 10\bar{1}0\rangle$ poles were concentrated along the tension direction compared to the ED-Out as shown in Fig. 7(d). That was to say, the percentage of basal slip in the TD-Out was much lower than that in the ED-Out and prismatic slip would be preferred in more grains of the TD-Out. This result was also verified in Figs. 8 and 9 which showed the fractions for $(10\bar{1}0)$ and $(11\bar{2}0)$ planes rotation induced by prismatic slip. As shown in Fig. 10, the fraction of prismatic slip was slightly higher than that of basal slip due to the texture characteristic in the TD sample which exhibited strong basal texture. Therefore, basal slip in conjunction with the prismatic slip was the deformation mechanism in the TD-Out.

Compared with the texture evolution of ZK60 alloy in the literature [7], it should be noted that the texture evolution in the outer regions of Mg−Nd−Zn−Zr alloy during the bending process was different from that of ZK60, while the inner regions of two alloys were similar. As shown in Figs. 7(b, d), the (0002) pole figure in the ED-Out became more diffusive along the TD, and similarly the (0002) pole figure in the TD-Out became more diffusive along the ED, i.e., the *c*-axes rotated along the direction perpendicular to the tension direction and thus the texture became diffusively distributed. According to the literature [10], the addition of Nd element promoted the prismatic $\langle a\rangle$ slip, which led to the expansion of the basal poles perpendicular to the loading direction and the enhancement of the $\langle 10\bar{1}0\rangle$ pole along the loading direction.

3.5 Bending behavior

Figure 11 showed the strain-hardening curves of tension and compression tests, which could be an effective way to describe the deformation mechanism. In this study, the strain-hardening curves using the $d\sigma/d\varepsilon$–$(\sigma-\sigma_{0.2})$ plot were derived from flow curves in Fig. 3(a) for investigating the bending behavior, where σ, ε and $d\sigma/d\varepsilon$ referred to stress, strain and strain-hardening rate, respectively. ZHANG et al [24] reported that the positive slope of the curve, K_{tw}, could be used in strain-hardening curves to quantify twin-dominated deformation and the negative slope of the curve, K_{sl}, could be used to quantify slip-dominated deformation. It could be seen that the positive slope of strain-hardening rate for both ED sample and TD sample exhibited an increase in strain-hardening rate due to the reorientation of $\{10\bar{1}2\}$ tension twin, but it was replaced by a negative slope arising from the dislocation slip after the curve reached a local maximum. Moreover, the rising part of strain-hardening curves could be divided into two stages and the positive slopes of different stages were denoted by K_{tw1} and K_{tw2}, respectively. As shown in Fig. 11, K_{tw1} reached 88.3 and 68.5 for the ED sample and TD sample respectively at the first stage and K_{tw2} reduced to 9.5 and 12.2 for the ED sample

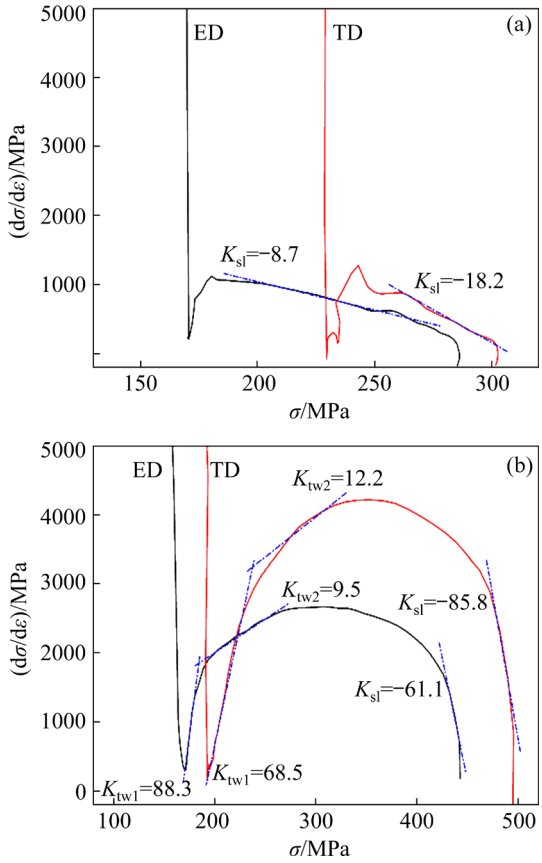

Fig. 11 Strain-hardening curves arising from tension (a) and compression (b) tests for ED and TD samples

and TD sample respectively at the second stage. Compared with the strain-hardening curves of ZK60 in the literature [7], the decrease of K_{tw} at the second stage might be ascribed to the rare earth elements in Mg−Nd−Zn−Zr. The differences between the ED sample and the TD sample in the values of K_{sl} and K_{tw} were attributed to the initial texture which influenced the activation of $\{10\bar{1}2\}$ tension twin. According to the literature [25], the length of rising part was closely related to the volume fraction of grains favoring $\{10\bar{1}2\}$ tension twin and increased with increasing quality of $\{10\bar{1}2\}$ tension twin. It could be seen that the TD sample with strong basal texture activated more $\{10\bar{1}2\}$ tension twins which resulted in a longer length of rising part (corresponding to K_{tw1} of 68.5 and K_{tw2} of 12.2). When the twin volume fraction reached saturation, i.e. the strain-hardening rate achieved the maximum, a transition from twinning to slip-dominated flow took place [26]. Clearly, the TD sample that remained strong twin texture possessed a lower K_{sl} of −85.8 than that in the ED sample. CHEN et al [27] suggested that the negative slope had a strong dependence on texture and became milder as the basal intensity weakened. That was to say, this phenomenon was also ascribed to the initial texture. Thus, the prior deformation mechanism in the inner region of the bending sample was twin-induced deformation, and subsequently transformed into slip-dominated deformation, and its priority was affected by initial texture state. Due to the strong basal texture, the massive activation of $\{10\bar{1}2\}$ tension twin allowed the TD sample to maintain a high strain-hardening capacity and was the fundamental reason for the higher bending stress in this sample.

It should be noted that the strain-hardening curves of uniaxial tension test in Fig. 11(a) also had a rising part of strain-hardening rate. According to the literature [28], these strain-hardening rate curves indicated that some twins might be formed at the early stage of tensile deformation. When the strain-hardening rate reached its maximum value, consistent with previous work, it meant that the twins were nearly exhausted. The deformation of subsequent descending stage was dominated by dislocation slip. Similarly, compared with the ED sample, the TD sample with strong basal texture had a lower negative slope, corresponding to the K_{sl}=−18.2. That was to say, the deformation mechanism in the outer region of the bending samples was dominated by dislocation slip, and the influence of the texture still played a leading role. Therefore, the differences of the strain-hardening rate were ascribed to the effects of initial texture and deformation mode, and the priority of deformation mechanism was dependent on the initial texture. Therefore, the differences in strain-hardening rates were attributed to the influence of the deformation mode and initial texture, and the preference of the deformation mechanism depended on the initial texture.

4 Conclusions

(1) The difference in the distribution of the bimodal basal texture along the ED and the TD led to the asymmetry in the bending behavior, and the TD sample with strong basal texture had higher bending stress.

(2) The microstructure characteristics showed that the dislocation density and the percentage of LAGBs in the outer region of the bending samples

were larger than those in the inner region, and those in the inner region of the TD sample were lower than those in the inner region of the ED sample, which was mainly caused by the bimodal texture in the initial texture. The activation of $\{10\bar{1}2\}$ tension twins in the inner region of the TD sample reduced the emergence propensity of high dislocation density and low angle grain boundaries.

(3) The initial texture ultimately played an important role in the evolution of the texture by influencing the deformation mechanisms in the inner region and the outer region of samples during the bending process. For the ED sample with weak basal texture, the dominant deformation mechanisms were basal slip in the majority with minor supplement of $\{10\bar{1}2\}$ tension twins in the inner region while basal slip and prismatic slip in the outer region. By comparison, the strong basal texture in the TD sample activated more $\{10\bar{1}2\}$ tension twins in the inner region and more prismatic slips in the outer region.

(4) The strain-hardening curves extracted from tension and compression tests illustrated that the deformation mechanism depended on the initial texture. The massive activation of $\{10\bar{1}2\}$ tension twins allowed the TD sample to maintain a high strain-hardening capacity and was the fundamental reason for the higher bending stress in this sample.

Acknowledgments

This work was supported by National Natural Science Foundation of China (Nos. 51975146, 52205344), the Natural Science Foundation of Shandong Province, China (No. ZR2020QE171), the Key Research and Development Plan in Shandong Province, China (No. 2019JZZY010364), and the National Defense Basic Scientific Research of China (No. JCK2018603C017).

References

[1] WANG Hai-xuan, ZHANG Li-xin, CHEN Wen-zhen, FANG Da-qing, ZHANG Wen-cong, CUI Guo-rong. Improved tension/compression asymmetry achieved in high-strength magnesium alloys via compression-extrusion process [J]. Materials Science and Engineering: A, 2018, 736: 239−247.

[2] HU Li, LV Hu-yuan, SHI Lai-xin, CHEN Yu, CHEN Qiang, ZHOU Tao, LI Min-gao, YANG Ming-bo. Research on deformation mechanism of AZ31 magnesium alloy sheet with non-basal texture during uniaxial tension at room temperature: A visco-plastic self-consistent analysis [J]. Journal of Magnesium and Alloys, 2022, 10: 1994−2008.

[3] CHEN Xue-min, CHEN Wen-zhen, ZHANG Li-xin, WANG Hai-xuan, WANG Wen-ke, ZHANG Wen-cong. Combined-extrusion techniques for fabricating yield-symmetric ZK61 magnesium alloys rods focusing on texture influence on their mechanical responses [J]. Journal of Materials Processing Technology, 2021, 297: 117236.

[4] SINGH J, KIM M S, CHOI S H. The effect of strain heterogeneity on the deformation and failure behaviors of E-form Mg alloy sheets during a mini-V-bending test [J]. Journal of Alloys and Compounds, 2017, 708: 694−705.

[5] WANG Wen-ke, MA Li-min, CHAI Shao-chun, ZHANG Wen-cong, CHEN Wen-zhen, FENG Yang-ju, CUI Guo-rong. Role of one direction strong texture in stretch formability for ZK60 magnesium alloy sheet [J]. Materials Science and Engineering: A, 2018, 730: 162−167.

[6] SINGH J, KIM M, LEE J, GUIM H, CHOI S. Microstructure evolution and deformation behaviors of E-form and AZ31 Mg alloys during ex-situ mini-V-bending tests [J]. Journal of Alloys and Compounds, 2019, 778: 124−133.

[7] WANG Wen-ke, ZHANG Wen-cong, CHEN Wen-zhen, CUI Guo-rong, WANG Er-de. Effect of initial texture on the bending behavior, microstructure and texture evolution of ZK60 magnesium alloy during the bending process [J]. Journal of Alloys and Compounds, 2018, 737: 505−514.

[8] ZHAO Si-cong, GUO Er-jun, CAO Guo-jian, WANG Li-ping, LUN Yu-chao, FENG Yi-cheng. Microstructure and mechanical properties of Mg−Nd−Zn−Zr alloy processed by integrated extrusion and equal channel angular pressing [J]. Journal of Alloys and Compounds, 2017, 705: 118−125.

[9] HABIB S A, KHAN A S, GNÄUPEL-HEROLD T, LLOYD J T, SCHOENFELD S E. Anisotropy, tension-compression asymmetry and texture evolution of a rare-earth-containing magnesium alloy sheet, ZEK100, at different strain rates and temperatures: Experiments and modeling [J]. International Journal of Plasticity, 2017, 95: 163−190.

[10] HA Chang-wan, BOHLEN J, YI S, ZHOU Xiao-hua, BROKMEIER H, SCHELL N, LETZIG D, KAINER K U. Influence of Nd or Ca addition on the dislocation activity and texture changes of Mg−Zn alloy sheets under uniaxial tensile loading [J]. Materials Science and Engineering: A, 2019, 761: 138053.

[11] WANG Li-fei, LI Yong-qiao, ZHANG Hua, ZHANG Zheng-yong, YANG Qing-shan, ZHANG Qiang, WANG Hong-xia, CHENG Wei-li, SHIN K S, VEDANI M. Review: Achieving enhanced plasticity of magnesium alloys below recrystallization temperature through various texture control methods [J]. Journal of Materials Research and Technology, 2020, 9(6): 12604−12625.

[12] DONG Jing-ren, ZHANG Ding-fei, SUN Jing, DAI Qing-wei, PAN Fu-sheng. Effects of different stretching routes on microstructure and mechanical properties of az31b magnesium alloy sheets [J]. Journal of Materials Science & Technology, 2015, 31(9): 935−940.

[13] HOU De-wen, ZHU Yu-zhi, WEN Hai-ming. Roles of twinning and $\langle a \rangle$ slipping in tensile anisotropy of rolled Mg−3Al−Zn alloy [J]. Materials Science and Engineering: A, 2021, 823: 141748.

[14] CUI Chao, ZHANG Wen-cong, CHEN Wen-zhen, HE Jian, CHEN Xue-min, HOU Jia-bin. Microstructure, texture

evolution and yield strength symmetry improvement of as-extruded ZK60 Mg alloy via multi-directional impact forging [J]. Journal of Magnesium and Alloys, 2022, 10: 2745−2760.

[15] HONG S, PARK S H, LEE C S. Role of $\{10\bar{1}2\}$ twinning characteristics in the deformation behavior of a polycrystalline magnesium alloy [J]. Acta Materialia, 2010, 58(18): 5873−5885.

[16] GUI Yun-wei, CUI Yu-jie, BIAN Hua-kang, LI Quan-an, OUYANG Ling-xiao, CHIBA A. Role of slip and $\{10\bar{1}2\}$ twin on the crystal plasticity in Mg−RE alloy during deformation process at room temperature [J]. Journal of Materials Science & Technology, 2021, 80: 279−296.

[17] WAN Zhi-peng, SHEN Jing-yuan, WANG Tao, WEI Kang, LI Zhao, YAN Sen, LIU Meng, HU Lian-xi. Effect of hot deformation parameters on the dissolution of γ' precipitates for as-cast Ni-based superalloys [J]. Journal of Materials Engineering and Performance, 2022, 31(2): 1594−1606.

[18] SAHOO S K, BISWAS S, TOTH L S, GAUTAM P C, BEAUSIR B. Strain hardening, twinning and texture evolution in magnesium alloy using the all twin variant polycrystal modelling approach [J]. International Journal of Plasticity, 2020, 128: 102660.

[19] FRYDRYCH K, LIBURA T, KOWALEWSKI Z, MAJ M, KOWALCZYK-GAJEWSKA K. On the role of slip, twinning and detwinning in magnesium alloy AZ31B sheet [J]. Materials Science and Engineering: A, 2021, 813: 141152.

[20] GUAN Bo, XIN Yun-chang, HUANG Xiao-yu, WU Pei-dong, LIU Qing. Quantitative prediction of texture effect on Hall−Petch slope for magnesium alloys [J]. Acta Materialia, 2019, 173: 142−152.

[21] CHAPUIS A, LIU Qing. Simulations of texture evolution for HCP metals: Influence of the main slip systems [J]. Computational Materials Science, 2015, 97: 121−126.

[22] WANG Wen-ke, CHEN Wen-zhen, ZHANG Wen-cong, CUI Guo-rong, WANG Er-de. Effect of deformation temperature on texture and mechanical properties of ZK60 magnesium alloy sheet rolled by multi-pass lowered-temperature rolling [J]. Materials Science and Engineering: A, 2018, 712: 608−615.

[23] WANG Y N, HUANG J C. Texture analysis in hexagonal materials [J]. Materials Chemistry and Physics, 2003, 81(1): 11−26.

[24] ZHANG W C, YU Y, ZHANG X N, CHEN W Z, WANG E D. Mechanical anisotropy improvement in ultrafine-grained ZK61 magnesium alloy rods fabricated by cyclic extrusion and compression [J]. Materials Science and Engineering: A, 2014, 600: 181−187.

[25] WANG Bing-shu, XIN Ren-long, HUANG Guang-jie, LIU Qing. Effect of crystal orientation on the mechanical properties and strain hardening behavior of magnesium alloy AZ31 during uniaxial compression [J]. Materials Science and Engineering: A, 2012, 534: 588−593.

[26] HAN G, NOH Y, CHAUDRY U M, PARK S H, HAMAD K, JUN T. $\{10\bar{1}2\}$ extension twinning activity and compression behavior of pure Mg and Mg−0.5Ca alloy at cryogenic temperature [J]. Materials Science and Engineering: A, 2022, 831: 142189.

[27] CHEN W Z, WANG X, WANG E D, LIU Z Y, HU L X. Texture dependence of uniform elongation for a magnesium alloy [J]. Scripta Materialia, 2012, 67(10): 858−861.

[28] LEE S W, KIM S, JO W, HONG W, KIM W, MOON B G, PARK S H. Twinning and slip behaviors and microstructural evolutions of extruded Mg−1Gd alloy with rare-earth texture during tensile deformation [J]. Journal of Alloys and Compounds, 2019, 791: 700−710.

双峰基面织构对 Mg−2.6Nd−0.55Zn−0.5Zr 合金弯曲应力及显微组织演变的影响

张文丛，刘宇轩，马俊飞，王文珂，陈文振，刘欣彤，杨建雷

哈尔滨工业大学(威海) 材料科学与工程学院，威海 264209

摘　要：沿 Mg−2.6Nd−0.55Zn−0.5Zr 板材挤压方向(ED)和横向(TD)分别切取试样，研究双峰基面织构对其弯曲应力及显微组织演变的影响。结果显示，具有弱基面织构的 ED 试样比 TD 试样的弯曲应力低很多。这种各向异性是不同织构状态对变形机制及显微组织演变的作用所导致的。对于具有弱基面织构的 ED 试样，其主要的变形机制是基面滑移：内侧区域存在少量的 $\{10\bar{1}2\}$ 拉伸孪生，而外侧区域则是基面滑移和柱面滑移。相比之下，具有强基面织构的 TD 试样在内侧区域激活更多的 $\{10\bar{1}2\}$ 拉伸孪生，在外侧区域激活更多的柱面滑移。$\{10\bar{1}2\}$ 拉伸孪生的激活一方面促使〈0002〉//压缩方向类型的织构增加，使内侧区域的织构角度限制在±30°范围内，另一方面减少高位错密度和低角度晶界的出现几率。$\{10\bar{1}2\}$ 拉伸孪生的大量激活使 TD 试样保持高应变硬化能力，是该试样具有较高弯曲应力的根本原因。

关键词：Mg−Nd−Zn−Zr 合金；织构；拉伸孪生；三点弯曲；弯曲应力；显微组织演变

(Edited by Wei-ping CHEN)